CHEMISTRY OF MATERIALS

Article

Converting Hierarchical to Bulk Structure: A Strategy for Encapsulating Metal Oxides and Noble Metals in Zeolites

Jianjian Wang, Lingmei Liu, Xinglong Dong, Lujain Alfilfil, Chia-En Hsiung, Zhaohui Liu, and Yu Han

Chem. Mater., **Just Accepted Manuscript** • DOI: 10.1021/acs.chemmater.8b02403 • Publication Date (Web): 27 Aug 2018

Converting Hierarchical to Bulk Structure: A Strategy for Encapsulating Metal Oxides and Noble Metals in Zeolites

Jianjian Wang[1,2], Lingmei Liu[1], Xinglong Dong[1,2], Lujain Alfilfil[1], Chia-En Hsiung[1], Zhaohui Liu[1] & Yu Han[1,2*]

[1] King Abdullah University of Science and Technology (KAUST), Physical Sciences and Engineering Division (PSE), Advanced Membranes and Porous Materials Center, Thuwal 23955-6900, Saudi Arabia.

[2]King Abdullah University of Science and Technology (KAUST), Physical Sciences and Engineering Division (PSE), KAUST Catalysis Center, Thuwal 23955-6900, Saudi Arabia.

ABSTRACT

Encapsulating catalytically active components into zeolites is a way to prepare multifunctional catalysts with unique selectivity and enhanced stability. Previously reported methods for encapsulation were only suitable for encapsulating specific species with a limited loading capacity. Here, we report a general strategy for encapsulating various metal oxides in zeolites. Our strategy is based on the use of directly synthesized hierarchical zeolites with abundant intra-crystalline mesopores. Metal oxides that are preloaded in the mesopores by impregnation become encapsulated during a secondary growth process that converts the original hierarchical structure into a bulk structure of zeolite. This method enables the encapsulation of ultrafine particles (2-4 nm) of various metal oxides (CeO_2, TiO_2, and MnO_x) in zeolites with loading as high as > 10 wt%. Furthermore, we modify this method to achieve the encapsulation and high dispersion of noble metals (Au and Pt), which would otherwise agglomerate into large particles on the zeolite surfaces, by taking advantage of their strong interactions with metal oxides. The encapsulated metal oxides and metal oxide-supported noble metals demonstrate reactant selectivity, product selectivity, and excellent thermal stability during catalytic oxidation and hydrogenation reactions.

INTRODUCTION

Zeolites are widely used as catalysts and sorbents, and feature well-defined intra-crystalline micropores of molecular dimensions. Encapsulating catalytically active components in the zeolite structure is an effective means to disperse and stabilize them, as well as to integrate multiple functions in one catalyst that retains the unique size- and shape-selectivity of zeolites.[1-4] A variety of catalytic components, including noble metals,[5-26] non-noble transition metals,[27-37] metal oxides,[38-46] metal sulfides,[47] metal carbides,[48] and heteropolyacids,[49] have been encapsulated in zeolites by different methods.

Metals are usually introduced into pre-synthesized zeolites by an ion-exchange method, followed by the reduction or decomposition of the metal-organic complex.[50] The resulting metal clusters are confined to microporous cavities in the zeolite. This method requires that the zeolite has a high ion-exchange capacity and large pore openings that allow the solvated metal ions or metal complex precursors to pass through. Metal encapsulation *via* direct synthesis has also been reported, though the metal loading in zeolites achieved in this way is usually limited (< 1 wt%).[7] For example, Iglesia *et al*. used (3-mercaptopropyl)trimethoxysilane to carry metal (Pt, Pd, Ir, Rh, and Ag) ions into zeolites during a crystallization process.[6,8,18] A subsequent treatment by H_2 produced metal clusters residing in the microporous cavities. However, this method was only applied to LTA zeolites, possibly because other zeolites cannot accommodate alkylsilanes in their frameworks. A more robust method using ligand-stabilized metal cationic complexes to encapsulate noble metals into SOD, GIS, and MFI zeolites was later reported.[7,22]

While some studies reported the encapsulation of metal oxides in zeolites *via* post-synthesis procedures,[39-42] the direct mixing of metal oxide precursors with synthetic zeolite gels is more common. This method was applied to encapsulate RuO_2,[38] TiO_2,[43] CoO_x,[44,46] and MnO_x,[45] but the sizes of as-prepared metal oxide particles were much larger than the pore diameters of the zeolites, thus suggesting that the particles did not reside in the micropores. Also, this direct-mixing method cannot accommodate a high loading of metal oxides because the addition of excessive metal precursors in the synthetic gel might interfere with the crystallization of the zeolite. In fact, it is difficult to determine whether the metal oxide particles are encapsulated within the zeolite crystals or are simply supported on their surfaces. The most used

characterization tool, transmission electron microscopy (TEM), only gives a two-dimensional projection image and, thus, cannot unambiguously distinguish between the two scenarios. Therefore, whether the particles exhibit molecular sieving or size-selective effects during catalysis has been used as indirect evidence of successful encapsulation.

Here, we report a general and effective strategy for encapsulating metal oxides in zeolites. We begin with hierarchically structured zeolites. The mesopores of these hierarchical zeolites can accommodate metal oxide particles through incipient wetness impregnation. Then, during a "secondary growth" process, which converts the hierarchical zeolites to bulk zeolites, the pre-loaded metal oxide particles are consequently encapsulated in the final materials. In this method, we make use of the confinement effects of a large amount of mesopores to achieve a high loading of metal oxides (> 10 wt%) with ultrafine particle sizes (2-4 nm). To obtain direct evidence of the encapsulation, we cut the obtained composite material into thin slices using a focused ion beam (FIB) to observe the distribution of the metal oxide particles in the interior of the zeolite crystals by TEM. Remarkably, our method can be extended to encapsulate noble metals in zeolites through their strong metal-support interactions with the metal oxides without the need of using any organic stabilizing ligands.[6,8,22] We demonstrate the effectiveness of this method using various combinations of zeolites (MFI and BEA), metal oxides (CeO_2, TiO_2, and MnO_x), and noble metals (Pt and Au), and find that the as-prepared catalysts all exhibit molecular-sieving selectivity in a series of reactions.

EXPERIMENTAL SECTION

Syntheses of materials. Hierarchical ZSM-5 (MS-ZSM-5), Silicalite-1 (MS-Silicalite-1), and Beta (MS-Beta) samples were synthesized by following the procedures that we reported previously.[51-53] A synthetic gel of ZSM-5 was prepared as a precursor for "secondary growth": 0.0283 g of $Al_2(SO_4)_3 \cdot 16H_2O$, 10 mL of tetrapropylammonium hydroxide solution (15 wt%) and 6 mL of TEOS were mixed at room temperature with vigorously stirring for > 4 h. The synthetic gel of Silicalite-1 was prepared using the same recipe but without adding $Al_2(SO_4)_3 \cdot 16H_2O$. The synthetic gel of zeolite Beta was prepared with a similar procedure but different compositions: 0.19 g of $NaAlO_2$, 0.033 g of NaOH, 0.053 g of NaCl, 0.144 g of KCl, 10.24 g of

tetraethylammonium hydroxide solution (35%) and 2.95 g of fumed silica were mixed at room temperature with vigorously stirring for > 4 h.

To perform the secondary growth, the calcined MS-ZSM-5 sample was degassed in a sealed flask at 200 ^{o}C under vacuum for 2 h and then cooled down to the room temperature; the prepared ZSM-5 synthetic gel (with a volume equal to the total pore volume of MS-ZSM-5) was injected into the flask to impregnate the degassed MS-ZSM-5, and the mixture was stirred for 2 h; the resultant wet sample was taken out from the flask and transferred into an autoclave reactor that was then heated at 180 ^{o}C for 1 d; finally, the resultant sample (SG-ZSM-5) was calcined at 550 ^{o}C for 6 h. The SG-Silicalite-1 and SG-Beta samples were prepared *via* the same procedure except injecting the respective synthetic gel into the corresponding zeolite.

The supported catalyst, CeO_2/MS-ZSM-5, was prepared by incipient wetness impregnation. Typically, a desired amount of cerium nitrate solution in ethanol was dropped into the MS-ZSM-5 zeolite. Then the wet catalyst was stirred and dried at 60 ^{o}C for 4 h and calcined at 400 ^{o}C for 4 h to obtain the CeO_2/MS-ZSM-5 sample. Other supported catalysts, such as CeO_2/MS-Beta, TiO_2/MS-ZSM-5, MnO_x/MS-Silicatelite-1, Au/MS-ZSM-5, Au-CeO_2/MS-ZSM-5, Pt/MS-ZSM-5, and Pt-CeO_2/MS-ZSM-5, were prepared in a similar way but varying the metal/metal oxide precursors or the zeolite support.

The encapsulated catalyst, CeO_2@SG-ZSM-5, was prepared by the secondary growth process described above using CeO_2/MS-ZSM-5 instead of MS-ZSM-5 as the starting material. Other encapsulated catalysts, such as CeO_2@SG-Beta, TiO_2@SG-ZSM-5, MnO_x@SG-Silicatelite-1, Au@SG-ZSM-5, Au-CeO_2@SG-ZSM-5, Pt@SG-ZSM-5, Pt-CeO_2@SG-ZSM-5, and Pt-CeO_2@SG-Silicalite-1, were prepared in a similar way but using different supported catalyst as starting materials and different zeolite precursors for secondary growth, according to the desired compositions.

Characterizations. Powder X-ray Diffraction Patterns were recorded on using a Bruker D8 Advance instrument with Cu Kα radiation (λ = 0.1542 nm) operated at 40 kV and 40 mA. Argon adsorption and desorption isotherms were measured at liquid argon temperature (87K) on a Micromeritics 3-Flex apparatus. Prior to the adsorption analysis, all the samples were degassed under vacuum at 300 ^{o}C for 10 h. Transmission electron microscopy (TEM) and scanning transmission electron microscopy (STEM) were performed on an FEI-Titan ST electron

microscope operated at 300 kV. The percentages of external acid sites in various zeolite samples were determined by an established method.[53]

Catalytic reactions. The catalytic oxidations of toluene over MnO_x-based catalysts were performed in Parr high-pressure batch-autoclave reactors (25 mL). Typically, 0.27 g of urea and 0.1 mol% of MnO_x-based catalyst were mixed with 9 mL of toluene. Then the reactor was purged with oxygen for several times, and filled with 1.5 MPa of oxygen before heating. After reaction at 190 ^{o}C for 8 h, the reaction mixture was taken out from the reactor and analyzed by GC equipped with a FID detector. The yields of benzonitrile, benzamide and benzoic acid were determined based on the amount of urea, and *n*-dodecane was used as an internal standard. The other products include benzyl alcohol, benzaldehyde and some minor unidentified compounds.

The selective hydrogenation reactions of nitrobenzene and 1,3-dimethyl-2-nitrobenzene over Pt-based catalysts were also conducted in Parr high-pressure batch-autoclave reactors. Typically, 0.25 mmol of substrate and Pt-based catalyst (0.4 mol% based on nitro group) were mixed well with 8 mL of ethanol. After purging with hydrogen for several times, the reactor was filled with 1.0 MPa of hydrogen, heated to 120 ^{o}C under stirring. After 3 h, the reaction mixture was collected and analyzed by GC using *n*-dodecane as an internal standard.

The selective hydrogenation reactions of 4-bromo-nitrobenzene were carried out in the same reactors as well. Typically, 10 mL of toluene, 0.2 g of 4-bromo-nitrobenzene and Pt-based catalyst (0.2 mol% based on 4-bromo-nitrobenzene) were added into reactor. Then the autoclave was purged with hydrogen several times to remove air left inside the reactor. After reaction at 110 ^{o}C for 0.75 h with 1.0 MPa of hydrogen, the products and unreacted reactant were analyzed by GC using *n*-dodecane as an internal standard.

The carbon balance was approximately 92~95% in the oxidative reaction, with a little amount of macromolecules or polymer product generated due to the high reaction temperature, which was not counted in the calculation of product selectivity. The carbon balance was > 96% in in all the hydrogenation reactions.

RESULTS AND DISCUSSION

We previously reported the direct synthesis of hierarchically structured MFI (ZSM-5, TS-1, and Silicalite-1) and BEA (Beta) zeolites using cationic polymers as dual-function templates to direct the formation of crystalline zeolitic and disordered mesoporous structures simultaneously in a one-pot synthesis.[51-53] The obtained zeolites had highly open and interconnected mesopores that broke the zeolite frameworks into small (a few unit cells in thickness) yet continuous domains.[51,53] Previous studies aimed to prepare hierarchical zeolites by creating mesoporosity in bulk zeolite crystals. Here, we do the opposite. We convert directly synthesized hierarchical zeolites into bulk zeolites, with the aim of encapsulating catalytically active components (e.g., metal oxides and metal nanoparticles) in the zeolites during the conversion. We based this idea on observations of hierarchical zeolites undergoing secondary growth under hydrothermal conditions in the presence of a small amount of zeolite precursors. During this process, the ultra-small zeolitic domains in the hierarchical zeolites acted as seeds that induced the crystallization of the precursors. Consequently, they grew into larger crystallites, and the original inter-domain mesopores were eliminated, as demonstrated in Figure 1. It is worth noting that we used isometric impregnation (i.e., using a zeolite synthetic gel with a volume equal to the pore volume of hierarchical zeolite as the precursor) to confine the secondary growth within the seed crystals, because excessive precursors could lead to separate nucleation/growth of new zeolite crystals.

Powder X-ray diffraction (PXRD) patterns of hierarchical ZSM-5 showed that the secondary growth process did not induce the formation of phases other than ZSM-5, but it did cause more intense and sharper reflection peaks, indicating an increase in the crystallite size (Figure 1a). Accordingly, the mesoporosity of ZSM-5 significantly decreased, as revealed by the adsorption behaviors in the relative pressure (P/P_0) range of 0.1-0.8 in the Ar sorption isotherms (Figure 1b). Specific textural properties derived from the isotherms are presented in Table 1, which clearly show decreases in the surface area and pore volume and, thus, the elimination of the mesoporous structure during the secondary growth process. The TEM images in Figure 1c reveal that hierarchical ZSM-5 consisted of particles with a highly branched fibrous structure, and that the zeolitic domains were only several nanometers in size. After secondary growth, the particles became more compact because the fibers evolved into bigger crystals of tens of nanometers, leading to the disappearance of the original mesoporosity among the fibers (Figure 1d). According to an established base-titration method,[53-54] the secondary growth process significantly decreased the amount of external Brønsted acid sites accessible to molecules too

large to enter the 10-ring channels of ZSM-5 from 30% to 7% (Figure S2). Taken together, these results confirm that hierarchical ZSM-5, synthesized from a templating route, was converted to bulk ZSM-5 by the secondary growth process. Similar results were also obtained for hierarchical Beta (Figure 1e-1h & Table 1).

To simplify the descriptions, the hierarchical zeolites are denoted by the prefix "MS-" (e.g., MS-ZSM-5 and MS-Beta), and their bulk zeolite counterparts (after secondary growth) are denoted by the prefix "SG-" (e.g., SG-ZSM-5 and SG-Beta). The encapsulation of the metal oxide nanoparticles in zeolites was exemplified by using cerium dioxide (CeO_2) and MS-ZSM-5. First, CeO_2 nanoparticles were deposited in the mesopores of MS-ZSM-5 by the incipient wetness impregnation method (CeO_2/MS-ZSM-5). Then, a small amount of synthetic gel of ZSM-5 was introduced to fill up the mesopores. The resulting mixture was hydrothermally treated to encapsulate CeO_2 in SG-ZSM-5 (CeO_2@SG-ZSM-5) (see the scheme in Figure 2). High-angle annular dark field scanning transmission electron microscopy (HAADF-STEM) images of MS-ZSM-5, CeO_2/MS-ZSM-5, and CeO_2@SG-ZSM-5 are presented side by side in Figure 2a-2c for easy identification of the structural evolution, where the loading of CeO_2 in the final material was ~ 2 wt%. The images show that small CeO_2 particles (2-4 nm) were produced within the fibrous mesoporous structure of MS-ZSM-5 during impregnation (Figures 2b and 2e), and eventually became embedded in the bulk zeolite ZSM-5 after the secondary growth process (Figures 2c and 2f). These results indicate that the "hierarchical-to-bulk" conversion of ZSM-5 was not affected by the CeO_2 loading, which was further confirmed by Ar sorption (Table 1 & Figure S3).

The abundant mesoporosity in the directly synthesized hierarchical zeolites allowed a large amount of metal oxide particles to be encapsulated without agglomerating *via* the 'hierarchical-to-bulk' strategy. Figure 2d shows the HAADF-STEM image of a FIB-prepared thin slice (~ 70 nm) of CeO_2@SG-ZSM-5 with CeO_2 loading as high as 10 wt%. In comparison with Figure 2c, the image contrast in Figure 2d is significantly improved due to the reduced thickness of the specimen, and clearly shows the uniform distribution and high density of the CeO_2 nanoparticles throughout the specimen. More importantly, we observed the interior of CeO_2@SG-ZSM-5 while preparing the specimen by FIB, and the results provided direct evidence of encapsulation. Voids can be observed among the small zeolite crystals in Figure 2d because the FIB specimen is

a two-dimensional slice extracted from a CeO_2@SG-ZSM-5 particle. In the original particle, the zeolite crystals were actually interconnected three-dimensionally and compactly packed without much void space. This ensured that the incorporated metal oxide particles were shielded by the zeolite structure and not directly accessible from the outside. Notably, direct mixing of the cerium precursor with the zeolite synthetic gel followed by hydrothermal synthesis could not achieve encapsulation, but resulted in phase separation between CeO_2 and the zeolite at low CeO_2 loadings or no crystallization of zeolite at high CeO_2 loadings (Figure S4).

This synthesis strategy has been extended to the encapsulation of other metal oxides in MFI and BEA zeolites. Typical HAADF-STEM images of the obtained composite materials, including CeO_2@SG-Beta, TiO_2@SG-ZSM-5, and MnO_x@SG-Silicalite-1, are presented in Figure S5. To demonstrate the effect of encapsulation on product selectivity, we used MnO_x@SG-Silicalite-1 as a catalyst for the oxidative cyanation of toluene. The reaction was performed at 190 ^{o}C using molecular oxygen (1.5 MPa) as an oxidant and urea as a nitrogen source. The reaction was slow without a catalyst, yielding small amounts of benzonitrile (6%) and benzamide (5%) after 8 h (Figure 3). The supported catalyst, MnO_x/MS-Silicalite-1, showed a high catalytic activity; it produced benzonitrile (31%), benzamide (5%), and benzoic acid (22%) under the same conditions. By comparison, the encapsulated catalyst, MnO_x@SG-Silicalite-1, was similarly active but more selective, yielding benzonitrile (51%), benzamide (7%), and a negligible amount of benzoic acid (~ 0.5%), which is an undesirable product in this reaction (Figure 3). Given that benzamide and benzoic acid can be generated from benzonitrile through hydration and hydrolysis reactions (Scheme S1),[45,55] we attribute the high selectivity toward benzonitrile of MnO_x@SG-Silicalite-1 to the hydrophobic shell of Silicalite-1, which prevented the trace amounts of water in the system from participating in the reaction. This result is in good agreement with phenomena reported in the literature,[45] providing a testament to the successful encapsulation of catalytic active sites in this zeolite.

We attempted to use this synthetic strategy to encapsulate noble metals (e.g., Au and Pt) in zeolites, but did not succeed in obtaining ultrafine metal particles. As shown in the STEM images, the noble metal particles prepared on hierarchical zeolite supports using the incipient wetness impregnation method were large in size (tens of nanometers for Au and ~10 nm for Pt) even before the secondary growth process (Figures 4a-4b). This is because noble metals, unlike

metal oxides, have low Tammann temperatures and high surface energies; therefore, they tend to agglomerate into large particles when dispersed on inert supports like silicates. In order to obtain finer noble metal particles for encapsulation, we made use of strong metal-support interactions (SMSI) to restrain the growth of the noble metal particles by co-impregnating the metal precursor with a metal oxide precursor on the hierarchical zeolites prior to the secondary growth process. We confirmed the effectiveness of this strategy through XRD characterizations. The sample prepared without the co-impregnation treatment, Au@SG-ZSM-5 (0.2 wt% Au loading), showed intense diffraction peaks of Au (111) and Au (200) from large Au particles, in agreement with the HAADF-STEM results (Figure 4c). In contrast, the sample prepared using the co-impregnation method, Au-CeO_2@SG-ZSM-5 (0.2 wt% Au; 10 wt% CeO_2), showed hardly discernible diffraction peaks of Au, suggesting that the Au particles were very small in size (Figure 4c). Similar phenomena were observed for the combinations of Pt-CeO_2 (Figure 4d) as well. We characterized Pt-CeO_2@SG-ZSM-5 (0.2 wt% Pt; 10 wt% CeO_2) with HAADF-STEM. Due to the high content of CeO_2, the small amount of Pt, and their close contact, it was difficult to identify the individual Pt particles by imaging. Elemental mapping by energy dispersive X-ray (EDX) spectroscopy, on the other hand, revealed the presence and uniform distribution of Pt throughout the material (Figure 4e). These results confirm that the noble metals were incorporated into zeolites through SMSI enabled by metal oxides, which effectively suppressed the sintering of noble metal during impregnation/reduction and the subsequent secondary growth process.

The as-prepared Pt-CeO_2@SG-ZSM-5 was used as a catalyst for the hydrogenation of two model molecules, nitrobenzene and 1,3-dimethyl-2-nitrobenzene, and compared with the supported Pt catalyst, Pt-CeO_2/MS-ZSM-5. When nitrobenzene was used as the substrate, both catalysts gave full conversions with nearly 100% selectivity toward aniline under the reaction conditions. However, Pt-CeO_2@SG-ZSM-5 showed much less activity for the bulky substrate 1,3-dimethyl-2-nitrobenzene, as well as lower selectivity toward 2,6-dimethylaniline, than Pt-CeO_2/MS-ZSM-5 (conversion: 7% vs. 92%) (Figure 5). Likewise, compared to Pt-CeO_2/MS-Silicalite-I, Pt-CeO_2@SG-Silicalite-I exhibited similar activity in the hydrogenation of nitrobenzene, but markedly less activity in the hydrogenation of 1,3-dimethyl-2-nitrobenzene (Figure 5). The observed difference in catalytic behavior between the encapsulated and the supported catalysts can be attributed to the size-exclusion effect of the MFI zeolite structure,

which allowed the small substrate nitrobenzene to pass through, but blocked the bulky substrate 1,3-dimethyl-2-nitrobenzene. This size selectivity was only observed in the encapsulated catalysts, not the supported catalysts, providing further evidence that our method can be credited with successfully encapsulating these noble metals in a zeolite.

In addition to the size selectivity, the encapsulated Pt catalyst also demonstrated unique selectivity between different reducible groups in hydrogenation (Scheme S2). Table 2 shows the results from various Pt catalysts used in a selective hydrogenation reaction of 4-bromo-nitroarene. Under the chosen reaction conditions, the tested catalysts gave comparable substrate conversions (30-50%), but different product selectivities. A remarkable amount of the substrate underwent debromination over the supported Pt catalysts, Pt/MS-ZSM-5 and Pt-CeO_2/MS-ZSM-5, leading to undesired aniline with a selectivity of > 20%. In contrast, the encapsulated catalyst, Pt-CeO_2@SG-ZSM-5, exhibited nearly 100% selectivity toward 4-bromo-aniline. These results demonstrate that Pt encapsulated in the MFI zeolite favored the reduction of nitro groups over bromo groups. Similar phenomena have been documented in the literature and attributed to the confinement effect of the surrounding zeolite structure, which causes the sterically preferential adsorption of nitro groups on Pt sites.[23] It is worth noting that the zeolites used for supporting or encapsulating Pt were in their as-synthesized form (not converted to H-form), and might differ in acidity due to their different synthetic procedures. In order to rule out the possibility that the observed difference in product selectivity arise from the acidity of zeolites, we converted Pt/MS-ZSM-5 and Pt-CeO2@SG-ZSM-5 to the H-form by ion-exchange and tested them as catalysts again with the same reaction. The results (see Table S1) confirm that the product selectivity is not affected by the acidity of the zeolites but mainly determined by the status of metal sites ("supported" or "encapsulated").

Our encapsulation strategy also endowed the noble metal species with excellent stability so that they retained their properties under harsh conditions. For example, after a heating treatment at 600 °C for 6 h or a streaming treatment at 600 °C for 5 h, only weak and broad diffraction peaks associated with Pt emerged in the XRD patterns of Pt-CeO_2@SG-ZSM-5, indicating that the Pt particles remained very small and highly dispersed throughout the zeolite matrix (Figure S6). Accordingly, the thermally and hydrothermally treated Pt-CeO_2@SG-ZSM-5 retained the catalytic activity and high selectivity toward 4-bromo-aniline during a hydrogenation reaction of

4-bromo-nitroarene (Table 2). We presume that the high stability of the Pt species originates from both SMSI with CeO_2 and the confinement and protection offered by the zeolite matrix.

CONCLUSIONS

Whereas hierarchical structure is usually fabricated in zeolites in order to enhance molecular transport and accessibility to the acid sites, we demonstrate in this study that it can also be used to accommodate additional catalytic components for the subsequent encapsulation that is achieved by converting the hierarchical structure to the bulk structure. Using this method, we successfully encapsulate various metal oxide nanoparticles in zeolites with unusually high loading and good dispersion. Moreover, we demonstrate that this method offer an effective route to the encapsulation of noble metals in zeolite by making use of SMSI without requiring any organic ligands to capture metal species. The obtained composite materials exhibited unique catalytic selectivity and excellent stability during the model reactions. Our study provides an effective alternative for preparing zeolite-encapsulated catalysts.

ASSOCIATED CONTENT

Supporting Information. Electron microscopic images, Ar sorption isotherms, and XRD patterns of various catalyst samples; the determination of the amount of the external acid sites in MS-ZSM-5 and SG-ZSM-5; schemes of the catalytic reaction pathways.

Corresponding Author

* yu.han@kaust.edu.sa

ACKNOWLEDGMENT

This research was supported by the Baseline Research Funding and Centre Competitive Research Funding to Y. H. from King Abdullah University of Science and Technology.

REFERENCES

1 Gounder, R.; Iglesia, E. The catalytic diversity of zeolites: confinement and solvation effects within voids of molecular dimensions. *Chem. Commun.* **2013**, *49*, 3491-3509.

2 Tian, H.; Li, X.; Zeng, L.; Gong, J. Recent Advances on the Design of Group VIII Base-Metal Catalysts with Encapsulated Structures. *ACS Catal.* **2015**, *5*, 4959-4977.

3 Farrusseng, D.; Tuel, A. Perspectives on zeolite-encapsulated metal nanoparticles and their applications in catalysis. *New J. Chem.* **2016**, *40*, 3933-3949.

4 Sadjadi, S.; Heravi, M. M. Pd(0) encapsulated nanocatalysts as superior catalytic systems for Pd-catalyzed organic transformations. *RSC Adv.* **2016**, *6*, 88588-88624.

5 Creyghton, E. J.; vanDuin, A. C. T.; Jansen, J. C.; Kooyman, P. J.; Zandbergen, H. W.; vanBekkum, H. Synthesis of Pt clusters in zeolite BEA - Effect of reduction rate on cluster size and location. *J. Chem. Soc., Faraday Trans.* **1996**, *92*, 4637-4642.

6 Choi, M.; Wu, Z. J.; Iglesia, E. Mercaptosilane-Assisted Synthesis of Metal Clusters within Zeolites and Catalytic Consequences of Encapsulation. *J. Am. Chem. Soc.* **2010**, *132*, 9129-9137.

7 Goel, S.; Wu, Z.; Zones, S. I.; Iglesia, E. Synthesis and catalytic properties of metal clusters encapsulated within small-pore (SOD, GIS, ANA) zeolites. *J. Am. Chem. Soc.* **2012**, *134*, 17688-17695.

8 Im, J.; Shin, H.; Jang, H.; Kim, H.; Choi, M. Maximizing the catalytic function of hydrogen spillover in platinum-encapsulated aluminosilicates with controlled nanostructures. *Nat. Commun.* **2014**, *5*, 3370.

9 Li, S.; Boucheron, T.; Tuel, A.; Farrusseng, D.; Meunier, F. Size-selective hydrogenation at the subnanometer scale over platinum nanoparticles encapsulated in silicalite-1 single crystal hollow shells. *Chem. Commun.* **2014**, *50*, 1824-1826.

10 Gu, J.; Zhang, Z.; Hu, P.; Ding, L.; Xue, N.; Peng, L.; Guo, X.; Lin, M.; Ding, W. Platinum Nanoparticles Encapsulated in MFI Zeolite Crystals by a Two-Step Dry Gel Conversion Method as a Highly Selective Hydrogenation Catalyst. *ACS Catal.* **2015**, *5*, 6893-6901.

11 Li, S.; Tuel, A.; Meunier, F.; Aouine, M.; Farrusseng, D. Platinum nanoparticles entrapped in zeolite nanoshells as active and sintering-resistant arene hydrogenation catalysts. *J. Catal.* **2015**, *332*, 25-30.

12 Rubio-Marques, P.; Rivero-Crespo, M. A.; Leyva-Perez, A.; Corma, A. Well-Defined Noble Metal Single Sites in Zeolites as an Alternative to Catalysis by Insoluble Metal Salts. *J. Am. Chem. Soc.* **2015**, *137*, 11832-11837.

13 Sibi, M. G.; Rai, A.; Anand, M.; Farooqui, S. A.; Sinha, A. K. Improved hydrogenation function of Pt@SOD incorporated inside sulfided NiMo hydrocracking catalyst. *Catal. Sci. Technol.* **2016**, *6*, 1850-1862.

14 Liu, L.; Diaz, U.; Arenal, R.; Agostini, G.; Concepcion, P.; Corma, A. Generation of subnanometric platinum with high stability during transformation of a 2D zeolite into 3D. *Nat. Mater.* **2017**, *16*, 132-138.

15 Wang, Q.; Han, W.; Lyu, J.; Zhang, Q.; Guo, L.; Li, X. In situ encapsulation of platinum clusters within H-ZSM-5 zeolite for highly stable benzene methylation catalysis. *Catal. Sci. Technol.* **2017**, *7*, 6140-6150.

16 Laursen, A. B.; Hojholt, K. T.; Lundegaard, L. F.; Simonsen, S. B.; Helveg, S.; Schuth, F.; Paul, M.; Grunwaldt, J. D.; Kegnaes, S.; Christensen, C. H.; Egeblad, K. Substrate size-selective catalysis with zeolite-encapsulated gold nanoparticles. *Angew. Chem. Int. Ed.* **2010**, *49*, 3504-3507.

17 Mielby, J.; Abildstrom, J. O.; Wang, F.; Kasama, T.; Weidenthaler, C.; Kegnaes, S. Oxidation of bioethanol using zeolite-encapsulated gold nanoparticles. *Angew. Chem. Int. Ed.* **2014**, *53*, 12513-12516.

18 Otto, T.; Ramallo-López, J. M.; Giovanetti, L. J.; Requejo, F. G.; Zones, S. I.; Iglesia, E. Synthesis of stable monodisperse AuPd, AuPt, and PdPt bimetallic clusters encapsulated within LTA-zeolites. *J. Catal.* **2016**, *342*, 125-137.

19 Saxena, S.; Singh, R.; Pala, R. G. S.; Sivakumar, S. Sinter-resistant gold nanoparticles encapsulated by zeolite nanoshell for oxidation of cyclohexane. *RSC Adv.* **2016**, *6*, 8015-8020.

20 Liu, C.; Liu, J.; Yang, S.; Cao, C.; Song, W. Palladium Nanoparticles Encapsulated in a Silicalite-1 Zeolite Shell for Size-Selective Catalysis in Liquid-Phase Solution. *ChemCatChem* **2016**, *8*, 1279-1282.

21 Wang, C.; Wang, L.; Zhang, J.; Wang, H.; Lewis, J. P.; Xiao, F. S. Product Selectivity Controlled by Zeolite Crystals in Biomass Hydrogenation over a Palladium Catalyst. *J. Am. Chem. Soc.* **2016**, *138*, 7880-7883.

22 Wang, N.; Sun, Q.; Bai, R.; Li, X.; Guo, G.; Yu, J. In Situ Confinement of Ultrasmall Pd Clusters within Nanosized Silicalite-1 Zeolite for Highly Efficient Catalysis of Hydrogen Generation. *J. Am. Chem. Soc.* **2016**, *138*, 7484-7487.

23 Zhang, J.; Wang, L.; Shao, Y.; Wang, Y.; Gates, B. C.; Xiao, F. S. A Pd@Zeolite Catalyst for Nitroarene Hydrogenation with High Product Selectivity by Sterically Controlled Adsorption in the Zeolite Micropores. *Angew. Chem. Int. Ed.* **2017**, *56*, 9747-9751.

24 Zhao, Z.; Li, Y.; Feyen, M.; McGuire, R.; Müller, U.; Zhang, W. Pd Nanoparticles Encapsulated in FER Zeolite through a Layer Reassembling Strategy as Shape-selective Hydrogenation Catalyst. *ChemCatChem* **2018**, *10*, 2254-2259.

25 Zahmakıran, M.; Özkar, S. Zeolite confined nanostructured dinuclear ruthenium clusters: preparation, characterization and catalytic properties in the aerobic oxidation of alcohols under mild conditions. *J. Mater. Chem.* **2009**, *19*, 7112-7118.

26 Yang, X.; Liu, Q.; Zhang, Y.; Su, X.; Huang, Y.; Zhang, T. In situ synthesis of metal clusters encapsulated within small-pore zeolites via a dry gel conversion method. *Nanoscale* **2018**, *10*, 11320-11327.

27 Aydin, C.; Lu, J.; Shirai, M.; Browning, N. D.; Gates, B. C. Ir6 Clusters Compartmentalized in the Supercages of Zeolite NaY: Direct Imaging of a Catalyst with Aberration-Corrected Scanning Transmission Electron Microscopy. *ACS Catal.* **2011**, *1*, 1613-1620.

28 Jiang, N.; Yang, G.; Zhang, X.; Wang, L.; Shi, C.; Tsubaki, N. A novel silicalite-1 zeolite shell encapsulated iron-based catalyst for controlling synthesis of light alkenes from syngas. *Catal. Commun.* **2011**, *12*, 951-954.

29 Dai, C.; Zhang, A.; Luo, L.; Zhang, X.; Liu, M.; Wang, J.; Guo, X.; Song, C. Hollow zeolite-encapsulated Fe-Cu bimetallic catalysts for phenol degradation. *Catal. Today* **2017**, *297*, 335-343.

30 Li, S.; Tuel, A.; Laprune, D.; Meunier, F.; Farrusseng, D. Transition-Metal Nanoparticles in Hollow Zeolite Single Crystals as Bifunctional and Size-Selective Hydrogenation Catalysts. *Chem. Mater.* **2015**, *27*, 276-282.

31 Han, J.; Cho, J.; Kim, J.-C.; Ryoo, R. Confinement of Supported Metal Catalysts at High Loading in the Mesopore Network of Hierarchical Zeolites, with Access via the Microporous Windows. *ACS Catal.* **2018**, *8*, 876-879.

32 Cimenler, U.; Joseph, B.; Kuhn, J. N. Hydrocarbon steam reforming using Silicalite-1 zeolite encapsulated Ni-based catalyst. *AIChE J.* **2017**, *63*, 200-207.

33 Laprune, D.; Tuel, A.; Farrusseng, D.; Meunier, F. C. Highly Dispersed Nickel Particles Encapsulated in Multi-hollow Silicalite-1 Single Crystal Nanoboxes: Effects of Siliceous Deposits and Phosphorous Species on the Catalytic Performances. *ChemCatChem* **2017**, *9*, 2297-2307.

34 Goodarzi, F.; Kang, L. Q.; Wang, F. R.; Joensen, F.; Kegnaes, S.; Mielby, J. Methanation of Carbon Dioxide over Zeolite-Encapsulated Nickel Nanoparticles. *ChemCatChem* **2018**, *10*, 1566-1570.

35 Wang, C.; Feng, S.; Liu, L.; He, Q.; Dong, J. A facile route to encapsulate ultrasmall Ni clusters within the pore channels of AlPO-5. *Mater. Lett.* **2018**, *210*, 211-213.

36 Zahmakiran, M.; Akbayrak, S.; Kodaira, T.; Ozkar, S. Osmium(0) nanoclusters stabilized by zeolite framework; highly active catalyst in the aerobic oxidation of alcohols under mild conditions. *Dalton Trans.* **2010**, *39*, 7521-7527.

37 Baekelant, W.; Aghakhani, S.; Coutino-Gonzalez, E.; Grandjean, D.; Kennes, K.; Jonckheere, D.; Fron, E.; d'Acapito, F.; Longo, A.; Lievens, P.; Roeffaers, M. B. J.; Hofkens, J. Confinement of Highly Luminescent Lead Clusters in Zeolite A. *J. Phys. Chem. C* **2018**, *122*, 13953-13961.

38 Zhan, B. Z.; Iglesia, E. RuO2 clusters within LTA zeolite cages: consequences of encapsulation on catalytic reactivity and selectivity. *Angew. Chem. Int. Ed.* **2007**, *46*, 3697-3700.

39 Liu, X. S.; Iu, K. K.; Thomas, J. K. Encapsulation of TiO2 in Zeolite Y. *Chem. Phys. Lett.* **1992**, *195*, 163-168.

40 Grubert, G.; Stockenhuber, M.; Tkachenko, O. P.; Wark, M. Titanium oxide species in molecular sieves: Materials for the optical sensing of reductive gas atmospheres. *Chem. Mater.* **2002**, *14*, 2458-2466.

41 Zhang, G.; Choi, W.; Kim, S. H.; Hong, S. B. Selective photocatalytic degradation of aquatic pollutants by titania encapsulated into FAU-type zeolites. *J. Hazard. Mater.* **2011**, *188*, 198-205.

42 El-Roz, M.; Lakiss, L.; El Fallah, J.; Lebedev, O. I.; Thibault-Starzyk, F.; Valtchev, V. Incorporation of clusters of titanium oxide in Beta zeolite structure by a new cold TiCl4-plasma process: physicochemical properties and photocatalytic activity. *Phys. Chem. Chem. Phys.* **2013**, *15*, 16198-16207.

43 Ma, R.; Wang, L.; Wang, S.; Wang, C.; Xiao, F.-S. Eco-friendly photocatalysts achieved by zeolite fixing. *Appl. Catal. B: Environ.* **2017**, *212*, 193-200.

44 Otto, T.; Zones, S. I.; Hong, Y.; Iglesia, E. Synthesis of highly dispersed cobalt oxide clusters encapsulated within LTA zeolites. *J. Catal.* **2017**, *356*, 173-185.

45 Wang, L.; Wang, G.; Zhang, J.; Bian, C.; Meng, X.; Xiao, F. S. Controllable cyanation of carbon-hydrogen bonds by zeolite crystals over manganese oxide catalyst. *Nat. Commun.* **2017**, *8*, 15240.

46 Liu, J.; Wang, Z.; Jian, P.; Jian, R. Highly selective oxidation of styrene to benzaldehyde over a tailor-made cobalt oxide encapsulated zeolite catalyst. *J. Colloid Interface Sci.* **2018**, *517*, 144-154.

47 Wang, Y.; Herron, N. Optical-Properties of Cds and Pbs Clusters Encapsulated in Zeolites. *J. Phys. Chem.* **1987**, *91*, 257-260.

48 Iida, T.; Shetty, M.; Murugappan, K.; Wang, Z.; Ohara, K.; Wakihara, T.; Román-Leshkov, Y. Encapsulation of Molybdenum Carbide Nanoclusters inside Zeolite Micropores Enables Synergistic Bifunctional Catalysis for Anisole Hydrodeoxygenation. *ACS Catal.* **2017**, *7*, 8147-8151.

49 Dai, C.; Zhang, A.; Li, J.; Hou, K.; Liu, M.; Song, C.; Guo, X. Synthesis of yolk-shell HPW@Hollow silicalite-1 for esterification reaction. *Chem. Commun.* **2014**, *50*, 4846-4848.

50 Ray, S.; Vasudevan, S. Encapsulation of cobalt phthalocyanine in zeolite-y: evidence for nonplanar geometry. *Inorg. Chem.* **2003**, *42*, 1711-1719.

51 Zhu, J.; Zhu, Y.; Zhu, L.; Rigutto, M.; van der Made, A.; Yang, C.; Pan, S.; Wang, L.; Zhu, L.; Jin, Y.; Sun, Q.; Wu, Q.; Meng, X.; Zhang, D.; Han, Y.; Li, J.; Chu, Y.; Zheng, A.; Qiu, S.; Zheng, X.; Xiao, F. S. Highly mesoporous single-crystalline zeolite beta synthesized using a nonsurfactant cationic polymer as a dual-function template. *J. Am. Chem. Soc.* **2014**, *136*, 2503-2510.

52 Liu, Z.; Dong, X.; Zhu, Y.; Emwas, A.-H.; Zhang, D.; Tian, Q.; Han, Y. Investigating the Influence of Mesoporosity in Zeolite Beta on Its Catalytic Performance for the Conversion of Methanol to Hydrocarbons. *ACS Catal.* **2015**, *5*, 5837-5845.

53 Tian, Q.; Liu, Z.; Zhu, Y.; Dong, X.; Saih, Y.; Basset, J.-M.; Sun, M.; Xu, W.; Zhu, L.; Zhang, D.; Huang, J.; Meng, X.; Xiao, F.-S.; Han, Y. Beyond Creation of Mesoporosity: The Advantages of Polymer-Based Dual-Function Templates for Fabricating Hierarchical Zeolites. *Adv. Funct. Mater.* **2016**, *26*, 1881-1891.

54 Liu, D.; Bhan, A.; Tsapatsis, M.; Al Hashimi, S. Catalytic Behavior of Brønsted Acid Sites in MWW and MFI Zeolites with Dual Meso- and Microporosity. *ACS Catal.* **2010**, *1*, 7-17.

55 Wang, Y.; Yamaguchi, K.; Mizuno, N. Manganese oxide promoted liquid-phase aerobic oxidative amidation of methylarenes to monoamides using ammonia surrogates. *Angew. Chem. Int. Ed.* **2012**, *51*, 7250-7253.

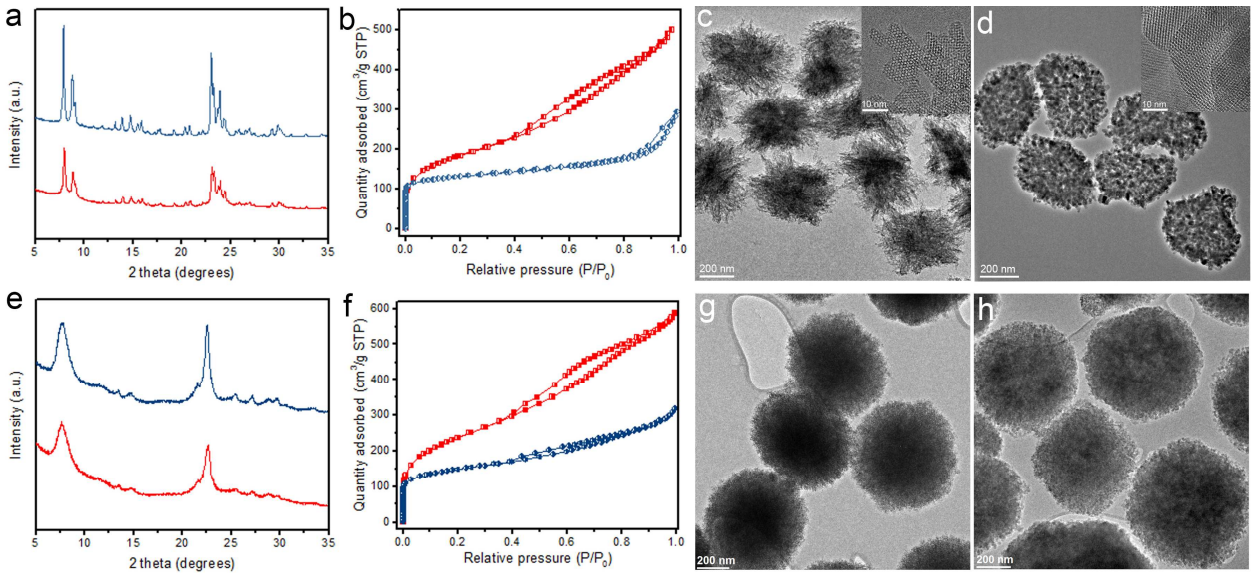

Figure 1. (a) PXRD patterns and (b) Ar sorption isotherms of hierarchical ZSM-5 before (red) and after (blue) secondary growth. (c-d) TEM images of hierarchical ZSM-5 before (c) and after (d) secondary growth. Insets in (c) and (d) are high-resolution images of the particle edges, showing ultra-thin branched zeolite domains in hierarchical ZSM-5 that develop into bigger crystals during secondary growth. (e) PXRD patterns and (f) Ar sorption isotherms of hierarchical Beta before (red) and after (blue) secondary growth. (g-h) TEM images of hierarchical Beta before (g) and after (h) secondary growth. High-resolution scanning transmission electron microscopic images of hierarchical Beta before and after secondary growth are shown in Figure S1.

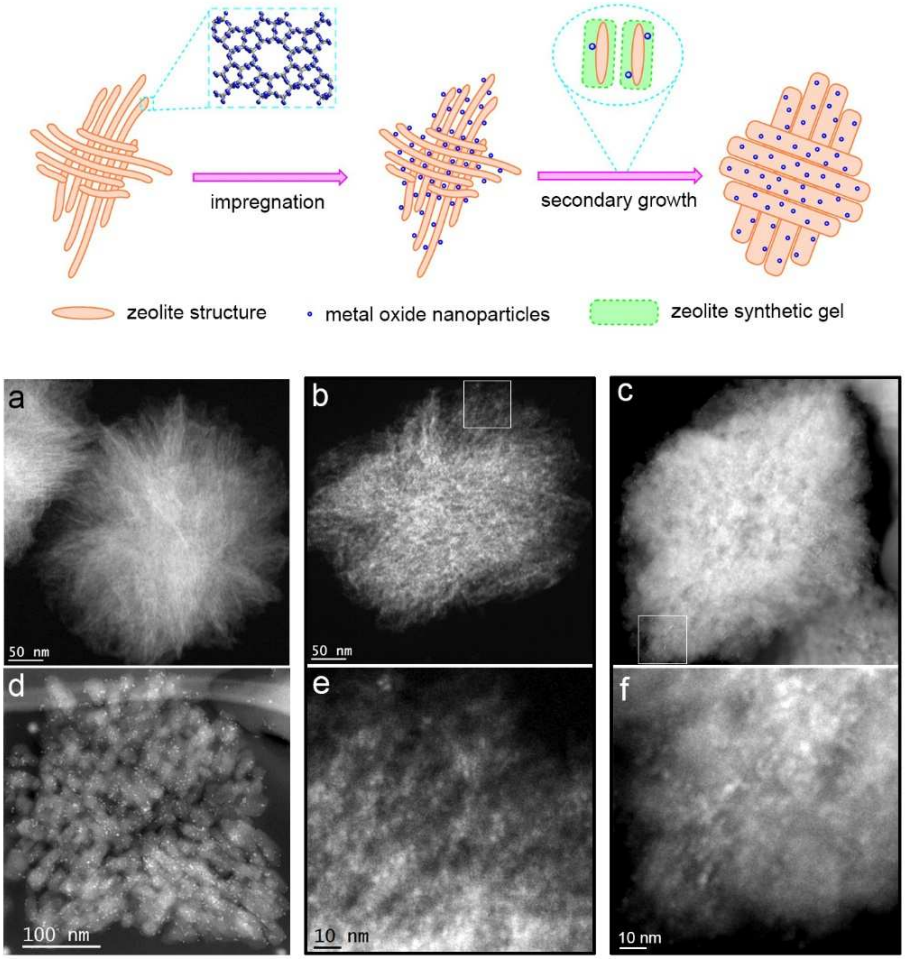

Figure 2. Schematic illustration and HAADF-STEM characterization of the encapsulation process. (a-c) HAADF-STEM images of MS-ZSM-5 (a), CeO_2/MS-ZSM-5 (b), and CeO_2@SG-ZSM-5 (c). The CeO_2 loading in (c) is 2 wt%. (d) HAADF-STEM image of a FIB-prepared specimen extracted from a CeO_2@SG-ZSM-5 particle with CeO_2 loading of 10 wt%. (e) Enlarged image of the highlighted area in (b) showing discrete ultrafine CeO_2 particles distributed throughout the mesoporous network of MS-ZSM-5. (f) Enlarged image of the highlighted area in (c) showing CeO_2 particles encapsulated by the secondary growth process.

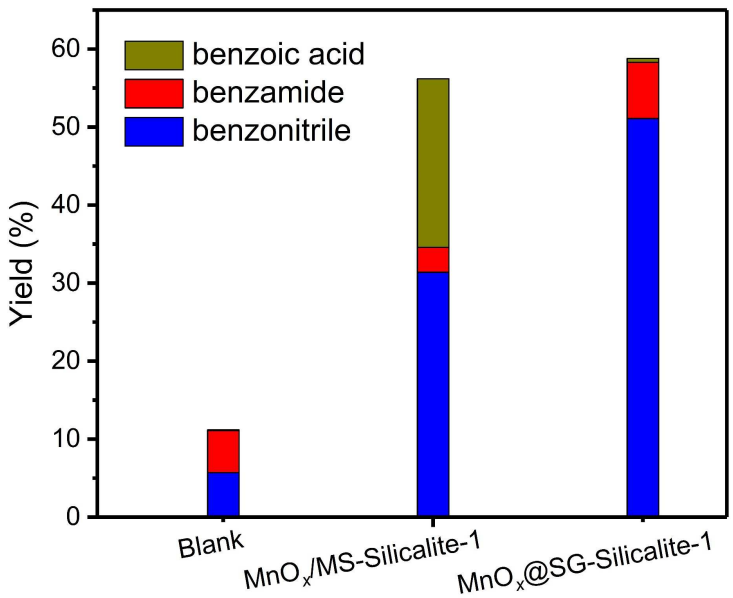

Figure 3. Results of catalytic oxidative cyanation of toluene to benzonitrile over MnO_x/MS-Silicalite-I and MnO_x@SG-Silicalite-I. The result of a blank experiment without a catalyst is also shown for comparison. Reaction conditions: 9 mL of toluene, 0.27 g of urea, 0.1 mol% of MnO_x-based catalyst, and 1.5 MPa of oxygen at 190 ^{o}C for 8 h; *n*-dodecane was used as the internal standard. Yields of the products were calculated based on the amount of nitrogen species in the urea.

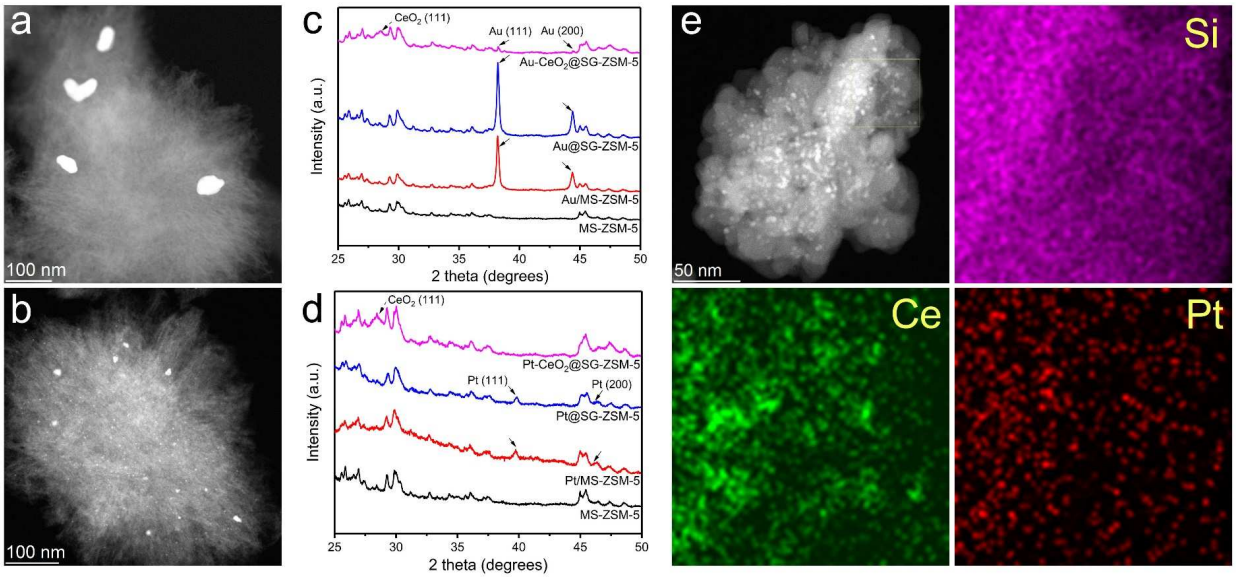

Figure 4. (a-b) HAADF-STEM images of (a) Au/MS-ZSM-5 and (b) Pt/MS-ZSM-5 (b) prepared by impregnation, showing the presence of large metal particles. (c-d) PXRD patterns of (c) different Au-containing and (d) Pt-containing ZSM-5 samples. The pattern of MS-ZSM-5 without loading metals is also shown for comparison. The diffraction peaks associated with CeO_2, Au and Pt are labelled by arrows. The results show that the co-impregnation of CeO_2 effectively suppresses the growth of metal particles, as evidenced by the much less intense diffraction peaks of metals in Au-CeO_2@SG-ZSM-5 and Pt-CeO_2@SG-ZSM-5 in comparison with their counterparts without CeO_2. (e) HAADF-STEM image and the results of EDX elemental (Si, Ce and Pt) mapping of the highlighted region, showing that Pt is highly dispersed throughout the sample.

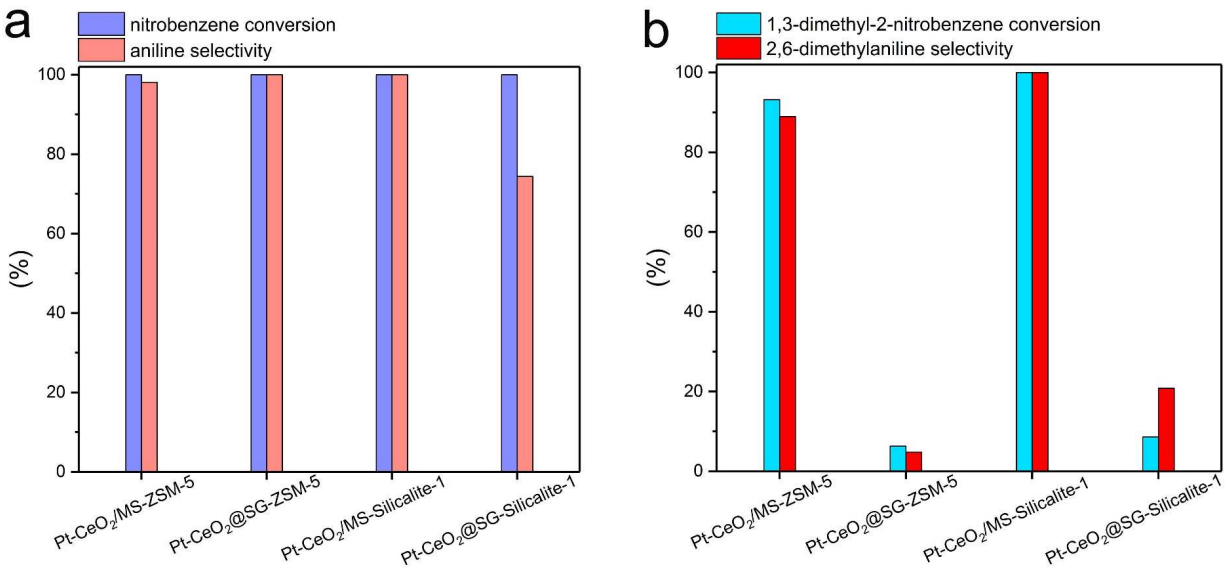

Figure 5. Results of selective hydrogenation of nitrobenzene (a) and 1,3-dimethyl-2-nitrobenzene (b) over different catalysts. Reaction conditions: 8 mL of ethanol, 0.25 mmol of substrate, 0.4 mol% of Pt-based catalyst, 1.0 MPa of hydrogen, 120 ^{o}C, 3 h, and *n*-dodecane used as internal standard.

Table 1 Textural properties of various samples derived from Ar sorption

	S_{BET} (m^2g^{-1})	V_{total}[a] (cm^3g^{-1})	V_{mic}[b] (cm^3g^{-1})	V_{meso}[c] (cm^3g^{-1})	V_{meso}/V_{total}
MS-ZSM-5	565	0.51	0.14	0.37	0.73
SG-ZSM-5	363	0.22	0.16	0.06	0.27
MS-Beta	723	0.62	0.20	0.42	0.68
SG-Beta	415	0.31	0.22	0.09	0.29
CeO_2/MS-ZSM-5	504	0.42	0.14	0.28	0.67
CeO_2@ZSM-5	359	0.25	0.15	0.10	0.40

[a] Single-point total pore volume at P/P_0 = 0.8. [b] Cumulative micropore (< 1 nm) volume determined from the NLDFT method using a cylinder model; [c] Difference between V_{total} and V_{mic}.

Table 2 Hydrogenation of 4-bromo-nitroarene over various catalysts. [a]

Entry	Catalyst	Conversion (%)[b]	Selectivity (%)[b]		
			4-Bromo-aniline	Nitrobenzene	Aniline
1[c]	-	4.6	0.0	0.0	5.6
2	Pt/MS-ZSM-5	42.8	63.7	0.5	25.7
3	Pt-CeO_2/MS-ZSM-5	53.1	75.1	0.8	23.1
4	Pt-CeO_2@SG-ZSM-5	42.6	> 99	0.5	1.0
5[d]	Pt-CeO_2@SG-ZSM-5-600 ^oC	45.2	> 99	0.2	0.6
6[e]	Pt-CeO_2@SG-ZSM-5-steamed	39.8	96.6	0.1	2.8

[a] Reaction conditions: 10 mL of toluene, 0.2 g of 4-bromo-nitrobenzene, 0.2 mol% of Pt-based catalyst, 1.0 MPa of hydrogen, 110 ^oC, 0.75 h. [b] Conversion of 4-bromo-nitrobenzene and products selectivity were calculated by using *n*-dodecane as internal standard. [c] Blank experiment without addition of catalyst. [d] Pt-CeO_2@SG-ZSM-5 sample was calcined at 600 ^oC for another 6 h in the air. [e] Pt-CeO_2@SG-ZSM-5 catalyst was treated with 10 vol.% steam in argon at 750 ^oC for 10 h.

Table of Contents